Available online at www.sciencedirect.com
SCIENCE DIRECT®
European Journal of Mechanics B/Fluids 24 (2005) 478–490

Vortex-induced vibrations and waves under shear flow with a wake oscillator model

L. Mathelin [a,b,*], E. de Langre [c]

[a] *LIMSI-CNRS, Université Paris-Sud, Orsay, France*
[b] *Institut Français du Pétrole, Rueil-Malmaison, France*
[c] *Département de Mécanique, LadHyX, École Polytechnique, Palaiseau, France*

Received 18 May 2004; received in revised form 8 December 2004; accepted 8 December 2004

Available online 16 March 2005

Abstract

This paper addresses the interaction of a slender structure and a sheared incident cross-flow. The oscillating wake of the structure is modeled using a distribution of van der Pol oscillators. Elementary configurations are first considered to assess the basic phenomena and structure dynamics allowing to reliably investigate more complex and realistic cases. The scope of the study thus ranges from a forced oscillating cylinder to a tensioned cable. This last configuration is found to experience wave-packets of vortex-induced motion due to a series of local lock-ins. A theoretical analysis is carried-out to predict the wave-packets amplitude and distribution. It is shown to be in reasonable agreement with the results of numerical simulations. This indicates that the system behavior can be described in terms of the *local* interactions between the wake and the structure only.

Keywords: VIV; VIW; Lock-in; Van der Pol; Fluid–structure interaction

1. Background

The vibrations induced by vortex (VIV) shedding from a slender mechanical structure have been studied for decades. This very common phenomenon, encountered in chimneys, offshore structures, towed marine devices, or buildings to cite just a few, can have powerful effects and lead to a significant weakening of the structure strength in a short period of time. In an engineering design process, it is thus essential to account for those effects. The reader may refer to the comprehensive review on the VIVs provided in [1].

In particular, experiments have provided significant insights, e.g. see [2–5] among many other. Besides the experimental approach, one of the first attempt to model the interaction between a structure and the flow considered the effect of the near wake through its phenomenological part [6,7]. The structure, described using classical cable or beam equations, was loaded by the wake reduced to its time-varying lift contribution. The true dynamics of the fluid part of the system was thus not resolved. This approach was proved successful in describing many experimentally observed behaviors. More recently, thanks to the steadily increasing computer power and the improvement of the numerical schemes, it has become possible to simulate

* Corresponding author. Tel.: +33 1 69 85 81 31; fax: +33 1 69 85 80 88.
E-mail addresses: mathelin@limsi.fr (L. Mathelin), delangre@ladhyx.polytechnique.fr (E. de Langre).

0997-7546/$ – see front matter
doi:10.1016/j.euromechflu.2004.12.005

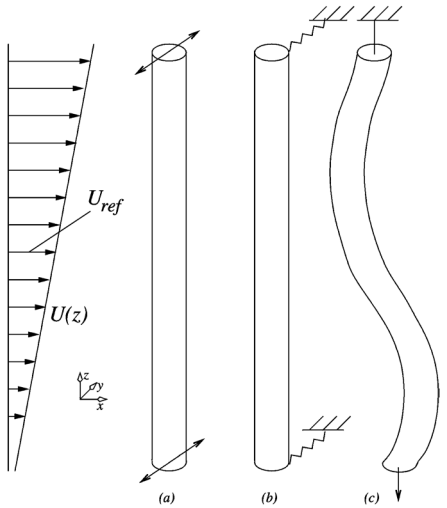

Fig. 1. Cable under shear flow. (a) forced rigid cable; (b) supported rigid cable; (c) tensioned cable.

realistic 2- or 3-D flows around various types of bodies. The entire fluid–structure system could then be accurately described and resolved with a minimum number of assumptions on the physics. The structure equations remained mainly the same while the fluid part was described in terms of Navier–Stokes equations using a LES model or even DNS [8–12]. A third, intermediate, approach consists in describing the wake using simple dynamical systems [13–18]. The main advantages are that such a simpler system is easier to understand and requires much less computer power to run. This is the approach retained in the present work following [19] and using van der Pol oscillators.

The aim of the present work is to analyze VIV configurations where several length scales interact, in particular when the incident flow profile is sheared, yielding a gradient length scale. Therefore the coupled dynamics between the wake and the structure should be considered in a global approach as opposed to a purely local approach which only depends on the local values of the variables.

The pulsation selection process proposed in [20] for a local interaction assumes a lock-in at the maximum oscillation amplitude for both the structure and the fluid. The current study should thus shed some light on how the system behaves for a global, and not only local, interaction. Does the selection mechanism proposed above hold true for the global system? How does a cable respond to a steeply-varying incident flow velocity?

In Section 2, the basic ingredients of the model are recalled. Cases of growing complexity are then considered through numerical simulations of the coupled wake and structure equations. The forced rigid cylinder under shear flow is first analyzed in Section 3. Then the cylinder is mounted on an elastic support to add a discrete degree of freedom, Section 4. Finally, a tensioned cable, Section 5, allows to address the case of a continuous structure where vortex-induced waves (VIW) are expected, as evidenced in [20].

2. Model description

2.1. Structure model

The model is here limited to cross-flow vibrations. The structure is assumed to be a tensioned cable of diameter D and lengthspan L_d submitted to an incident cross-flow of velocity $U(Z)$, Fig. 1. The displacement $Y(Z,T)$ of the cable is thus subjected to

$$m\partial^2_{TT}Y + R\partial_T Y - K\partial^2_{ZZ}Y = S \tag{1}$$

where K is the tension, S the forcing term due to the effects of the fluid onto the structure, T the time and Z the spanwise coordinate. The mass per unit length m is here the structural mass m_S enhanced with the effect of the fluid added mass m_f,

$$m = m_S + m_f = m_S + C_M \rho D^2 \frac{\pi}{4} \tag{2}$$

with ρ the fluid density and C_M the added mass coefficient. For a circular cylinder C_M is taken equal to 1.0 [2]. The parameter R accounts for the damping due to the structural viscous dissipation, R_S, and the added damping from the fluid, R_f,

$$R = R_S + R_f = R_S + \frac{1}{2}\rho D U C_D \tag{3}$$

with $C_D = 2.0$ [2], the drag coefficient for a circular cylinder in transverse motion. Hereafter we shall consider $m_S = 0$ and $R_S = 0$.

2.2. Wake model

Following [19], the wake of the flow past the structure is modeled using a distribution of non-linear van der Pol oscillators interacting in diffusion

$$\partial^2_{TT} q + \varepsilon \Omega_f (q^2 - 1)\partial_T q + \Omega_f^2 q - \nu_d \partial^3_{TZZ} q = F_d \tag{4}$$

where $\varepsilon = 0.3$ (see [19]), ν_d is a diffusion parameter, F_d is the forcing term due to the action of the structure onto the fluid and Ω_f is the incident flow pulsation depending on the local fluid velocity through the Strouhal law

$$\Omega_f = 2\pi St \frac{U}{D}. \tag{5}$$

The dimensionless variable $q(Z, T)$ may be associated with the transverse velocity of a representative near wake fluid mass [22].

2.3. Coupling between fluid and structure

In the model above, the fluid and the structure interact through the forcing terms. The effect of the wake oscillation, referred to using the variable q, is assumed to be proportional to its amplitude. The forcing term S is thus written as, [19],

$$S = \frac{1}{2}\rho U^2 D \frac{C_{L_0}}{2} q \tag{6}$$

where C_{L_0} is the lift coefficient when no vibrations occur, usually taken as $C_{L_0} = 0.3$ [2].

Similarly, the structure acts onto the fluid. In [19], it is shown that the best qualitative and quantitative agreement with experimental data is achieved when an inertial forcing term is considered, namely

$$F_d = \frac{A}{D}\partial^2_{TT} Y \tag{7}$$

with $A = 12$ as proposed after fitting with the data on the influence of the structure oscillation amplitude on the lock-in range in terms of pulsation.

For the sake of clarity, dimensionless variables are used hereafter. The cable diameter D, assumed to be constant along the whole cylinder span, provides a spatial length scale leading to

$$x = \frac{X}{D}, \quad y = \frac{Y}{D} \quad \text{and} \quad z = \frac{Z}{D}. \tag{8}$$

Unless specified the origin of the coordinates is set at the middle of the cable considered in the numerical domain. The time T is reduced considering a reference pulsation Ω_{ref} taken as the shedding pulsation at the middle of the numerical domain

$$\Omega_{\text{ref}} = 2\pi St \frac{U_{\text{ref}}}{D} \tag{9}$$

see Fig. 1. This leads to

$$t = T\Omega_{\text{ref}}. \tag{10}$$

Finally, Eqs. (1) and (4) are now expressed in dimensionless form as

$$\partial^2_{tt} y + r\partial_t y - c^2 \partial^2_{zz} y = M\omega_f^2 q, \tag{11}$$

$$\partial^2_{tt} q + \varepsilon\omega_f (q^2 - 1)\partial_t q + \omega_f^2 q - \nu \partial^3_{tzz} q = A\partial_{tt} y \tag{12}$$

where

$$\omega_f = \frac{\Omega_f}{\Omega_{\text{ref}}} = \frac{U}{U_{\text{ref}}}, \quad c = \frac{\sqrt{K/m}}{\Omega_{\text{ref}} D}, \quad \nu = \frac{\nu_d D^2}{\Omega_{\text{ref}}}, \quad L = \frac{L_d}{D},$$
$$M = \frac{C_{L_0}}{16\pi^2 St^2 \mu}, \quad \mu = \frac{m}{\rho D^2}, \quad r = \frac{R}{m\Omega_{\text{ref}}} = \frac{\gamma}{\mu}, \quad \gamma = \frac{C_D}{4\pi St} \simeq 0.8 \tag{13}$$

and the forcing terms now read

$$s = M\omega_f^2 q, \qquad F = A\partial_{tt}^2 y. \tag{14}$$

This model allows to reproduce many phenomena observed in experiments or high-accuracy numerical simulations: in addition to the lock-in extent, it was also proved successful to reproduce behaviors such as the hysteresis around lock-in, Griffin plots, dislocation cells in the wake, oblique vortex shedding, etc. See [19–21] for further details.

The system of Eqs. (11) and (12) is now solved numerically in space and time. The numerical method remains the same as in [20] where a centered finite differences scheme was applied both in time and space. In all cases considered in this paper, the regularity conditions on the wake variable q are set at the boundaries:

$$\partial_{zz}^2 q = 0. \tag{15}$$

3. Forced rigid cylinder

3.1. Lock-in cells

In this configuration, the cylinder is considered to move as a rigid body in a translation mode solely. The forcing of the fluid onto the structure is thus taken into account through its integral contribution along the whole lengthspan. The incident flow is steady in time and linearly sheared, Fig. 1(a), so that

$$U(Z) = U_{\text{ref}}\left(1 + \beta\frac{Z}{D}\right) \tag{16}$$

or in dimensionless pulsation form

$$\omega_f(z) = 1 + \beta z. \tag{17}$$

The incident flow shear parameter considered in this section is $\beta = 0.027$ [21] while the mass ratio μ is set equal to 0.79. The cylinder is forced at a unit dimensionless pulsation $\omega_{\text{Ext}} = 1$ chosen in order to match the shedding frequency at the center of the domain. The dimensionless structure amplitude y_0 is varied from 0 to 0.1. One therefore has

$$y(t) = y_0 \sin(\omega_{\text{Ext}} t). \tag{18}$$

The dimensionless lengthspan of the cylinder is here taken as $L = 50$ so that the dimensionless flow velocity varies from $0.325\,U_{\text{ref}}$ to $1.675\,U_{\text{ref}}$ from bottom to top.

When no fluid diffusion is considered, $\nu = 0$, the wake experiences a lock-in region of size λ_L around the unit pulsation region, Fig. 2. This appears on the contour levels of the power spectral density (PSD) field of the wake variable. Those contours are sharp as the PSD field is plotted with a logarithmic scale showing how peaked the wake response is in terms of frequency. Outside this lock-in region, the wake frequency is not locked and behaves as if the structure was essentially motionless. Its pulsation thus linearly varies with z. Lock-in is here defined by the condition that the dominant frequency in the wake PSD field is that of the forcing motion, $\omega_{\text{Ext}} = 1$. The size of the lock-in region λ_L shown in Fig. 2, is plotted in Fig. 3 as a function of the forcing amplitude y_0. This size λ_L regularly increases with the forcing amplitude y_0 as the range of lock-in along the z-axis may be associated to a range of flow velocity. This range of flow velocity can further be expressed in terms of reduced velocity $U_r = \omega_f/(St\,\omega_{\text{Ext}})$ and the range of lock-in in terms of U_r may therefore be plotted in terms of the forcing amplitude, y_0, Fig. 4. This is found to be consistent with the range of the lock-in of a 1-degree of freedom model estimated in [19] using a different criterion based on the lift enhancement. Actually, as no fluid diffusion is considered here, at each level of the z-axis the wake oscillator behaves as a forced oscillator $q(t)$. Therefore the results of this case of forced motion, Figs. 2 and 3, may be entirely interpreted by varying U_r as z is varied.

3.2. Diffusion cells

When a wake diffusion ν is considered, equation (12), the wake still experiences a lock-in region but the unlocked regions now exhibit dislocation cells, Fig. 5. Their size is constant over z and consistent with the theoretical result from [21], Fig. 6(a):

$$\lambda_C = 2\pi\sqrt{\frac{\nu}{\varepsilon}}. \tag{19}$$

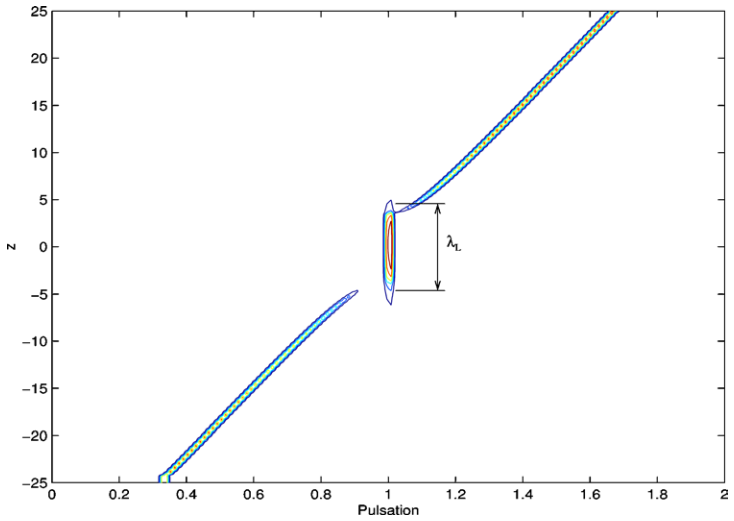

Fig. 2. Wake power spectral density field for $y_0 = 0.03$. Logarithmic scale on the contour levels of q_0. The lowest contour level is chosen so as to enhance the lock-in pattern.

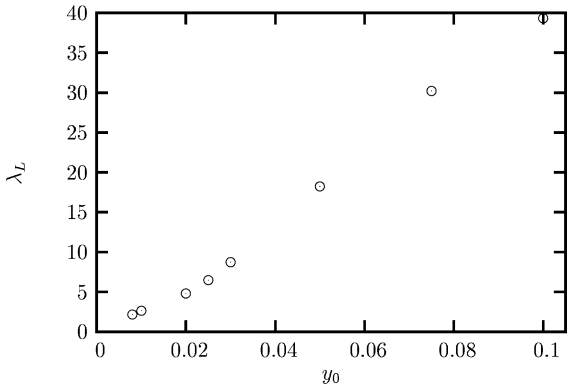

Fig. 3. Evolution of the lock-in region size λ_L with the forced amplitude.

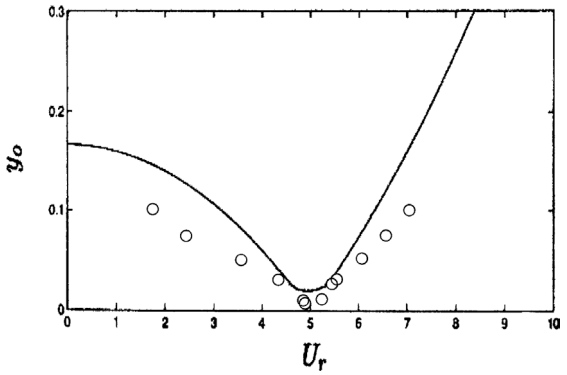

Fig. 4. Solid line, limits of the range of lift enhancement range extent (adapted from [19] on a 1-degree of freedom model); circles, boundaries of the lock-in range for the forced rigid cylinder, in terms of local reduced velocity.

From Fig. 6(a), this is seen to remain true for a viscosity value spanning from 0 to more than 0.1. For a higher viscosity, the size of the diffusion cells becomes of the order of the numerical domain. The agreement between the numerical results and the theoretical value of Eq. (19) shows that those cells are induced by diffusion and are thus not related to lock-in.

Fig. 6(b) presents the evolution of the lock-in region size when the diffusion parameter is varied. It is seen that the lock-in region grows approximately twice as fast as the size of the dislocation cells. At the edges between the lock-in and the unlocked regions, the nearest dislocation cell tends to merge with the lock-in region of length λ_{L_0} hence extending the size of the latter by almost λ_C. Occurring at the two edges, this phenomenon leads to an increase of λ_L of about $2\lambda_C$ so that we may approximate λ_L by

$$\lambda_L = \lambda_{L_0} + 2\lambda_C. \tag{20}$$

As diffusion and lock-in effects are found not to interact strongly here, all diffusive effects will be disregarded in the following sections of the paper.

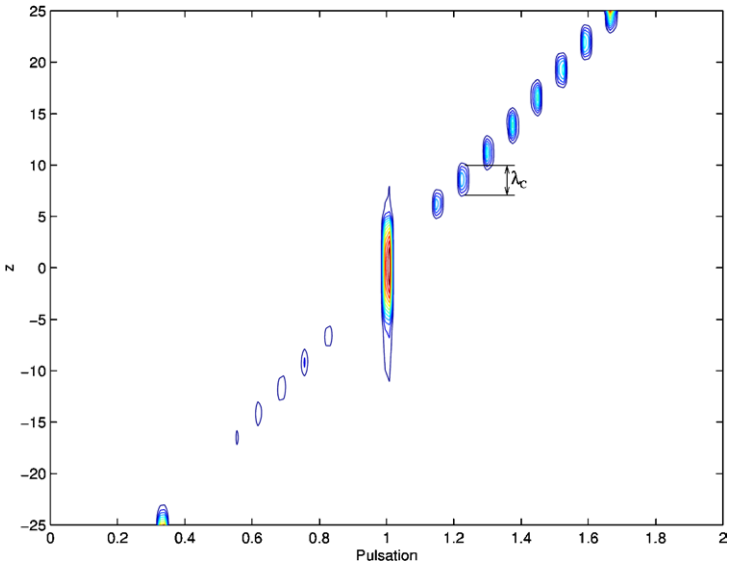

Fig. 5. Local wake power spectral density field. $y_0 = 0.03$, $\nu = 0.05$.

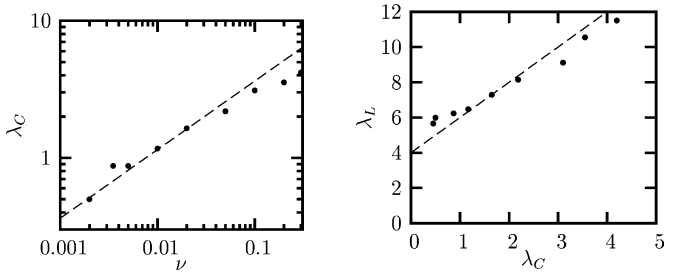

Fig. 6. Effect of wake diffusion. (a) Theoretical (dashed line) and numerical (dots) dislocation cells length with varying diffusion parameter ν. (b) Lock-in region size λ_L evolution with the dislocation cells size λ_C when diffusion is varied. $y_0 = 0.03$. The dashed line shows the approximate value given by Eq. (20).

4. Elastically supported rigid cylinder

The rigid cylinder is now elastically supported, Fig. 1(b), and coupled to the wake. Its dimensionless frequency appears as a new time scale in the dynamics. The structure dynamics is defined by

$$\partial_{tt}^2 y + r\,\partial_t y + \omega_S^2 y = s. \tag{21}$$

Again, the shear parameter is varied to study the effect of the shear incident flow onto the global system dynamics. The structure dynamics is set so as to have a unit cylinder pulsation $\omega_S = 1$ and thus a resonance with the incident flow shedding frequency at the middle of the domain. The amplitude of the resulting motion of the cylinder, y_0, is plotted in Fig. 7 as a function of the shear parameter β. For low shear values, the amplitude tends to the theoretical maximum amplitude at lock-in given by [19], namely

$$y_M = \frac{C_{L_0}/2}{4\pi^2 St^2 \gamma}\sqrt{1 + \frac{A}{\varepsilon}\frac{C_{L_0}/4}{4\pi^2 St^2 \gamma}} \tag{22}$$

leading to $y_M \simeq 0.218$. As the shear parameter increases, the amplitude progressively decreases and eventually vanishes beyond $\beta \simeq 0.013$ as shown in Fig. 8. This evolution may be interpreted by considering the size of the lock-in region λ_L, defined from the PSD of the wake variable as in the preceding section, in the following way:

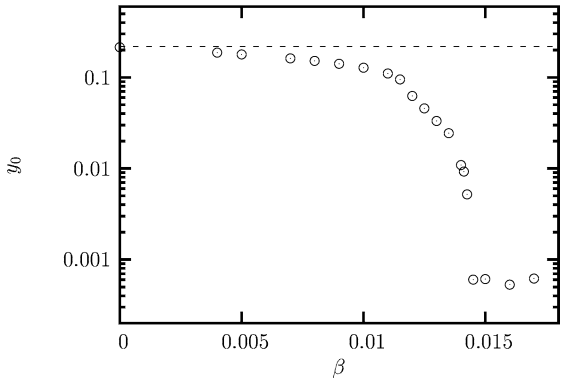

Fig. 7. Structure displacement amplitude evolution with the shear parameter. The dashed line indicates the theoretical value of $y_M = 0.218$.

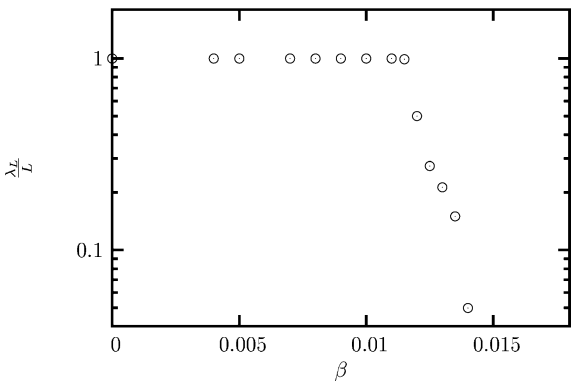

Fig. 8. Lock-in region extension evolution with the shear parameter.

(a) below $\beta = 0.012$ the whole wake is locked on the cylinder frequency, i.e. $\lambda_L/L = 1$. The amplitude slowly decreases with shear as the local difference between the cylinder frequency and that given by the Strouhal law increases. This is equivalent to the behavior of a 1-degree of freedom model as stated in [19],

(b) between $\beta = 0.012$ and 0.014 only a part of the wake is locked, i.e. $\lambda_L/L < 1$, Fig. 8. The contribution of the unlocked regions to the cylinder motion are negligible. Therefore, the amplitude steeply decays as does λ_L,

(c) at $\beta = 0.014$ lock-in disappears and the cylinder motion sets at a very small amplitude. This critical value of the shear parameter can be approximated by considering that, as shown in Fig. 4, a given level of cylinder amplitude can be associated with a given range of reduced velocity. This range covers all the cylinder length if the shear parameter is small enough. Considering a level of $y_0 = 0.1$, which is half the maximum value as a rough indicator of the limit of the lock-in regime, the corresponding extent of reduced velocity is about [1.8; 7.0]. Lock-in will be lost at the upper part of the cylinder first when $U_r^{\max} = 7.0$. As $U_r(L/2) = U_{r_{\text{ref}}}(1 + \beta L/2) = U_r^{\max}$, it leads to

$$1 + \beta(L/2) = U_r^{\max} St\, \omega_S \tag{23}$$

yielding $\beta = 0.016$. This is in reasonable agreement with the value $\beta = 0.014$ estimated from Fig. 7, further indicating that the core mechanism of lock-in is well illustrated by Fig. 4.

5. Tensioned cable

5.1. Wave-packets

In this last, most general, case, a semi-infinite domain is considered. The cylinder is assumed to be a tensioned cable, Fig. 1(c)

$$\partial_{tt}^2 y + r\,\partial_t y - c^2 \partial_{zz}^2 y = s. \tag{24}$$

The cable wave velocity c is set to be constant all over the spanlength. The spanwise numerical extent of the simulated system is set sufficiently large to contain several wavenumbers, if any, in the z-direction along the structure axis. The shear parameter is chosen as $\beta = 0.045$ in order to have a near vanishing velocity at the bottom of the z-axis. Here $L = 40$ and the z-axis is set at the bottom of the numerical domain. The fluid conditions remain the same as above while for the cable an absorbent boundary condition is set at $z = 0$

$$\partial_t y - c\partial_z y = 0 \tag{25}$$

and a clamped condition at the top, $y = 0$ for $z = L$.

It is seen in Fig. 9(a) that the wake exhibits several cells of constant pulsation and various extent most apparent in a PSD field form as shown in Fig. 10(a). Besides those cells, there exists an unlocked region where the fluid behaves as if the cylinder was motionless. It can also be seen from Figs. 9(b) and 10(b) that the structure exhibits the same patterns with several regions of precisely set discrete frequencies. The fluid and structure frequencies match each other indicating a local lock-in which occurs at the local fluid pulsation as deduced from Figs. 10(a) where the incident flow pulsation is plotted for comparison. Wave-packets

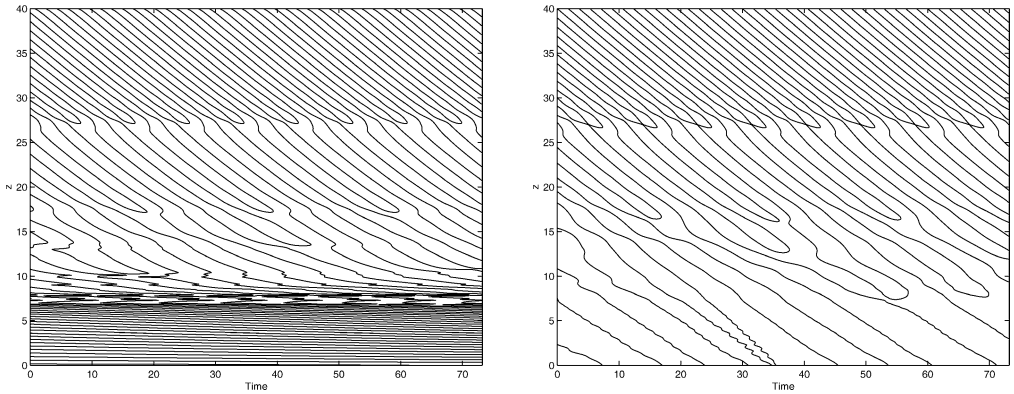

Fig. 9. Tensioned cable under shear flow. (a) Wake; (b) structure clamped at the top. Isolines of $q = 0$ and $y = 0$ respectively.

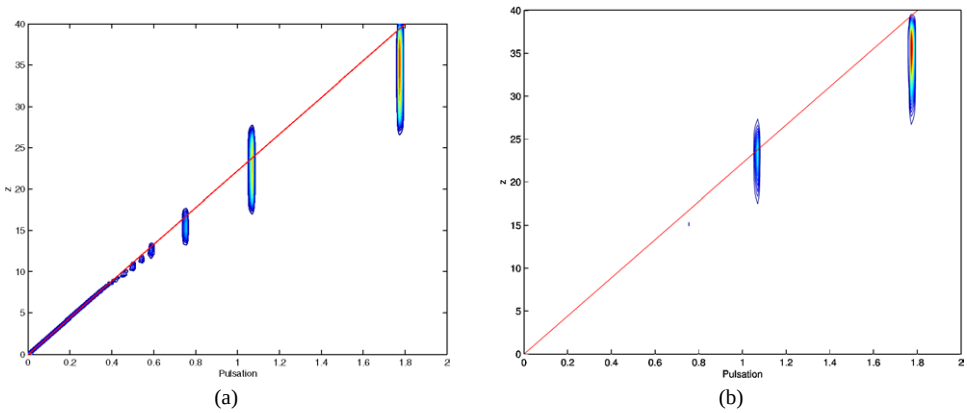

Fig. 10. Power spectral density field. The incident flow pulsation profile is plotted for comparison (solid line). (a) Wake; (b) structure.

cells are clearly centered around the local incident fluid pulsation and the system exhibits a discrete behavior with wave-packets occurring within each cell.

This behavior is confirmed by the evolution of the amplitude of the structure plotted in Fig. 11(a). The amplitude is defined here as the peak to peak value. It exhibits a bumpy profile, each bump corresponding to a cell location, confirming their local lock-in character. A typical instantaneous displacement is plotted in Fig. 11(b) showing the wave-packet pattern of the structure motion.

5.2. *Local lock-in model*

A theoretical analysis similar to [23] is now proposed to further shed some light on this particular behavior and to understand the main features and underlying mechanisms of the lock-in of the tensioned cable. Following [20], the coupled system is first considered

$$\begin{aligned} &\partial_{tt}^2 y + r\,\partial_t y - c^2 \partial_{zz}^2 y = M q \omega_f^2, \\ &\partial_{tt}^2 q + \varepsilon \omega_f \partial_t q (q^2 - 1) + \omega_f^2 q = A \partial_{tt}^2 y. \end{aligned} \tag{26}$$

The following derivation is parallel to that of [19], except that ω_f is here dependent on z and can not be set to 1 arbitrarily. The solutions are searched for in a traveling waves form: $y(z,t) = y_0\,\mathrm{e}^{\mathrm{i}(\omega t - kz)}$ and $q(z,t) = q_0\,\mathrm{e}^{\mathrm{i}(\omega t - kz + \phi)}$ with ϕ the phase lag between the structure and the wake movement. Substituting those waves forms in system (26) leads to

$$\begin{bmatrix} D_S(\omega,k) & -M\omega_f^2\,\mathrm{e}^{\mathrm{i}\phi} \\ \omega^2 A\,\mathrm{e}^{-\mathrm{i}\phi} & D_F(\omega,k;\omega_f) \end{bmatrix} \begin{pmatrix} y_0 \\ q_0 \end{pmatrix} = 0 \tag{27}$$

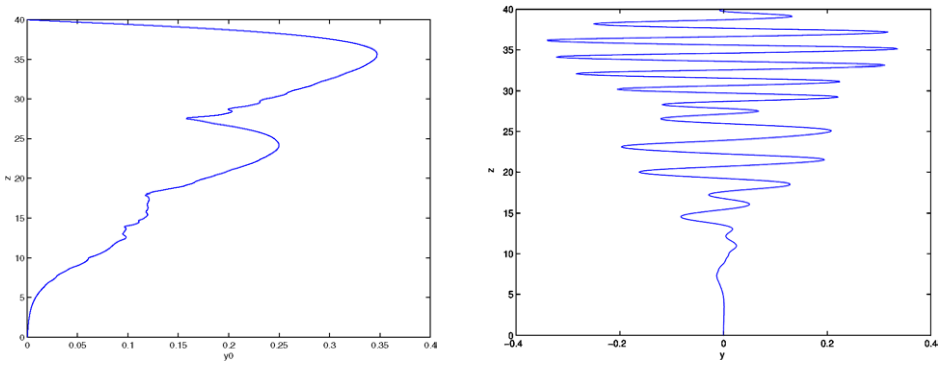

(a) (b)

Fig. 11. Structure motion. (a) Structure oscillation amplitude evolution in space; (b) typical structure displacement snapshot.

where $D_S(\omega,k)$ and $D_F(\omega,k;\omega_f)$ are the structure and fluid dispersion relations respectively expressed as, using a first order approximation in pulsation,

$$D_S(\omega,k) = (c^2k^2-\omega^2) + \mathrm{i}r\omega = 0, \tag{28}$$

$$D_F(\omega,k;\omega_f) = \omega_f^2 - \omega^2 + \mathrm{i}\varepsilon\omega_f\left(\frac{q_0^2}{4}-1\right) = 0. \tag{29}$$

To avoid trivial and physically meaningless solutions, the determinant of the matrix must be zero in Eq. (27) leading to

$$D_S(\omega,k)D_F(\omega,k;\omega_f) + AM\omega^2\omega_f^2 = 0. \tag{30}$$

The real part of this equation leads to the value of the wake amplitude

$$q_0^2 = 4\left[1 + \frac{\mu AM\omega_f}{\gamma\varepsilon} + \frac{\mu(c^2k^2-\omega^2)(\omega_f^2-\omega^2)}{\gamma\varepsilon\omega_f\omega^2}\right]. \tag{31}$$

Substituting q_0 in Eq. (30) gives the structure displacement amplitude

$$y_0^2 = q_0^2\frac{M^2\omega_f^4}{(c^2k^2-\omega^2)^2+\gamma^2\omega^2/\mu^2}. \tag{32}$$

The local maximum amplitude along the cable can be estimated by considering a resonance condition. This is done by simultaneously enforcing a vanishing real part for the structure and the wake dispersion relation, $\mathcal{R}[D_S(\omega,k)]=0$ and $\mathcal{R}[D_F(\omega,k;\omega_f)]=0$, leading to

$$\omega^2 = c^2k^2 \quad \text{and} \quad \omega^2 = \omega_f^2 \tag{33}$$

respectively. Substituting in Eqs. (31) and (32) yields

$$q_{\max}^2 = 4\left(1+\frac{\mu AM\omega_f}{\gamma\varepsilon}\right), \tag{34}$$

$$y_{\max}^2 = \frac{4\mu^2M^2\omega_f^2}{\gamma^2}\left(1+\frac{\mu AM\omega_f}{\gamma\varepsilon}\right). \tag{35}$$

These amplitudes are dependent on z as ω_f varies along the z-axis. The evolutions of $q_{\max}$ and $y_{\max}$ are plotted in Figs. 12(a) and 12(b). The amplitudes of q and y at the center of the wave-packet in the numerical simulations, are also plotted for comparison showing good agreement. This demonstrates that the selection mechanism proposed in [20] for a *uniform* incident flow still holds true for a shear flow: (a) as the structure dispersion relation does not impose any particular (ω,k) set, the wake selects its local oscillating frequency through the Strouhal law; (b) due to lock-in the structure then oscillates at the same frequency and selects the wavenumber according to its own dispersion relation; (c) the wavenumber is then imposed to the wake; (d) their respective amplitudes are derived from the dynamical equilibrium as a balance between forcing and damping terms. It is striking that here a model based on *local* properties solely is able to predict the whole amplitude distribution of both the wake and the structure variables.

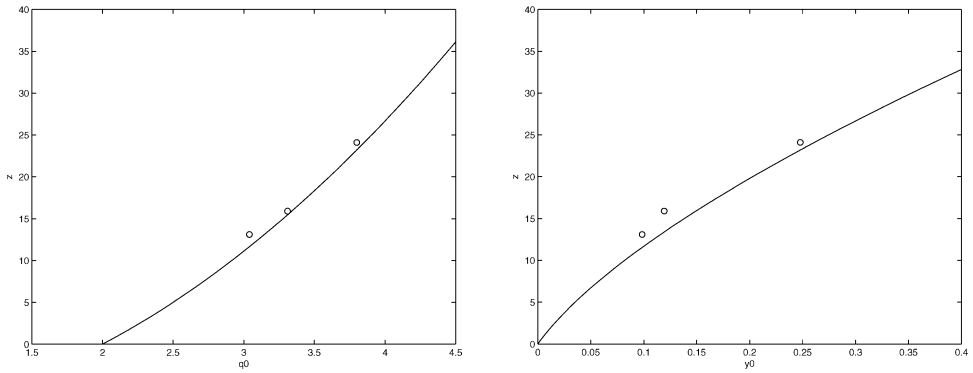

(a) (b)

Fig. 12. Oscillations envelop evolution along the cable. Comparison between the numerical simulation (open circles) and the theoretical model prediction (solid line), Eqs. (34) and (35). (a) Wake; (b) structure.

Several other features of the evolution of the wake and structure amplitude may also be understood using the local analysis. Considering the imaginary part of the dispersion relation (30) yields the relationship between the pulsation ω, the wavenumber k and the incident pulsation ω_f:

$$\omega^6 + \omega^4\left[-2c^2k^2 - \omega_f^2 + \frac{\gamma^2}{\mu^2} + AM\omega_f^2\right] + \omega^2\left[c^4k^4 + 2\omega_f^2c^2k^2 - \frac{\gamma^2\omega_f^2}{\mu^2} - AM\omega_f^2c^2k^2\right] - c^4k^4\omega_f^2 = 0. \tag{36}$$

Together with Eqs. (31) and (32), it allows to describe the q and y distribution in the general case where Eq. (33) does not necessarily hold. The corresponding theoretical prediction of the wake and structure motion is plotted in Fig. 13 in comparison with the result from the numerical simulations already seen in Fig. 11(a). The wave-packets, or bursts, are clearly reproduced and exhibit very similar features with those from the simulation.

The location of bursts is set by the boundary conditions. On the upper, clamped, boundary condition, a lock-in cell sets-in with an extent determined by the mechanisms described above. Once the amplitude in the first cell decays, a second, contiguous, cell can take place and so on up to the location where the incident flow pulsation and the cylinder motion amplitude are not high enough for a wave-packet cell to exist. Close to the upper boundary condition, the system is expected to exhibit a highly non-linear behavior and the theoretical model assumption most likely does not hold. A different approach was chosen to compare the simulated bursts with the theoretically predicted ones. The cells frequencies are first determined from the numerical simulations and then taken as the lock-in frequencies of the wave-packets. The bursts envelops are then predicted based on each lock-in frequency. The upper burst was not modeled.

Some insights on the bumpy character of the wake and cylinder motion distribution can further be proposed. Besides the maximum amplitude of the lock-in cell, the local fluid pulsation is slightly different from the lock-in pulsation and additional terms are to be accounted for, see Eqs. (31) and (32). The local contribution to the lock-in decreases as the local natural conditions do not match exactly the lock-in values. This is very similar to what was seen in Section 4 where the wake was less and less contributing to the lock-in as the shear parameter was increased. The resulting lock-in cell thus exhibits a bumpy profile centered around the lock-in condition, the width of which being set by the local frequency. The lock-in occurs within a fixed range of reduced velocity $U_r \in [U_r^{\min}; U_r^{\max}]$. This range, expressed in terms of pulsation, varies with the lock-in frequency as

$$\omega_f = U_r St\, \omega_{\text{lock-in}}. \tag{37}$$

The extent of the lock-in burst on the z-axis therefore increases with $\omega_{\text{lock-in}}$ and hence with z. This appears in Fig. 13 as wider and wider bursts from bottom to top.

5.3. Effect of damping

An alternative, potentially more realistic, pulsation-dependent expression for the fluid-added damping is now considered

$$r_f = \frac{\gamma\omega_f}{\mu}. \tag{38}$$

Using Eqs. (34) and (35) but now with $r = \omega_f\gamma/\mu$ instead of γ/μ still allows to predict the wake and structure amplitude, Fig. 14. The structure and wake global behavior remains similar, exhibiting wave-packets of well defined constant frequency. The main difference with Fig. 13 comes from the fact that the fluid-induced damping now depends on the local pulsation ω_f

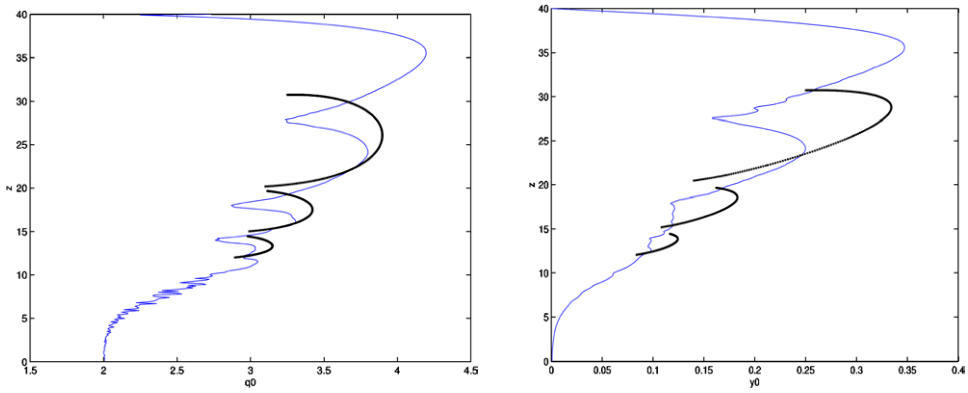

(a) (b)

Fig. 13. Oscillation amplitude distribution in terms of incident pulsation. Numerical simulation (thin line) and 1st order theoretical prediction (thick line). (a) Wake; (b) structure.

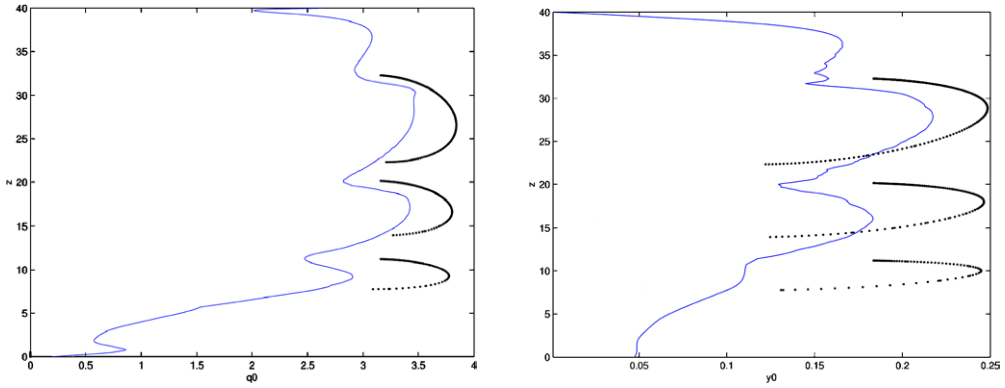

(a) (b)

Fig. 14. Oscillation amplitude distribution. Numerical simulation (thin line) and 1st order theoretical prediction (thick line). (a) Wake; (b) structure.

and is thus stronger in high frequency regions. It actually balances the increase of the forcing term from the fluid onto the structure which also increases with the local pulsation. This balance leads to an equilibrium where the wave-packet amplitude remains constant along z.

5.4. *Effect of the flow profile*

In this last section, a more realistic configuration is considered involving a slender flexible structure submitted to a steady spatially-varying incident shear flow. It is a coarse model of the external load encountered in facilities such as offshore risers or chimneys where a boundary layer is present and a velocity profile develops up to a free-stream value, here $U(z) = U_\infty(1 - \mathrm{e}^{-(3.9z/L+0.05)})$ with U_∞ the free-stream velocity chosen such as $\omega_{f_\infty} = 2.5$. The retained flow profile exhibits an exponential shape with a pulsation close to zero at the origin set at its bottom. The system is governed by Eqs. (26) and the fluid-added damping is that of Eq. (38).

As for preceding cases, the system is found to exhibit wave-packets patterns at precisely set frequencies along its lengthspan, Fig. 15. The wave-packets cells are distributed following the incident flow pulsation which is also plotted for comparison. As previously observed, the pulsation width of the cells decreases as the resonating pulsation increases, indicating that the above proposed mechanisms hold true for more general configurations.

Fig. 16 shows the amplitude of the wake and structure oscillation envelop. The theoretical prediction, though slightly shifted in frequency, is seen to remain reliable and to provide reasonable estimation of the structure amplitude, both qualitatively and quantitatively. Besides the wave-packets patterns, overshoots may be observed at the edges of both the structure and wake cells. They are also clearly noticeable when an instantaneous structure displacement snapshot is considered as in Fig. 17. This phenomenon certainly deserves further specific investigation.

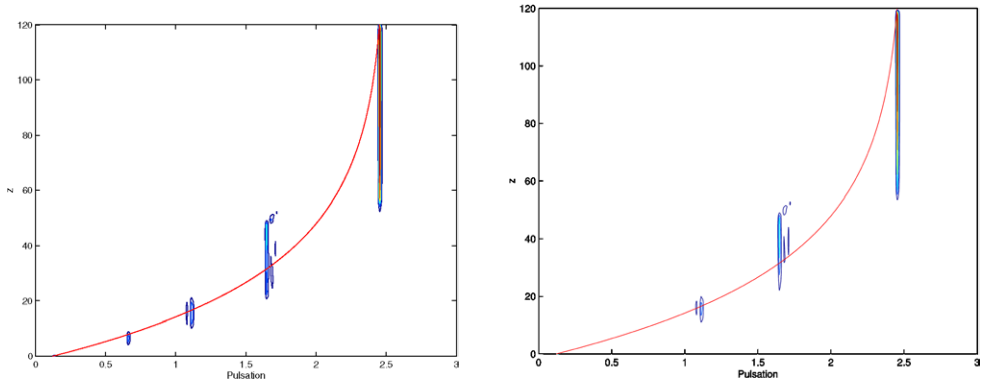

(a) (b)

Fig. 15. Power spectral density field. Boundary layer profile case. The incident flow pulsation profile is plotted for comparison (solid line). (a) Wake; (b) structure.

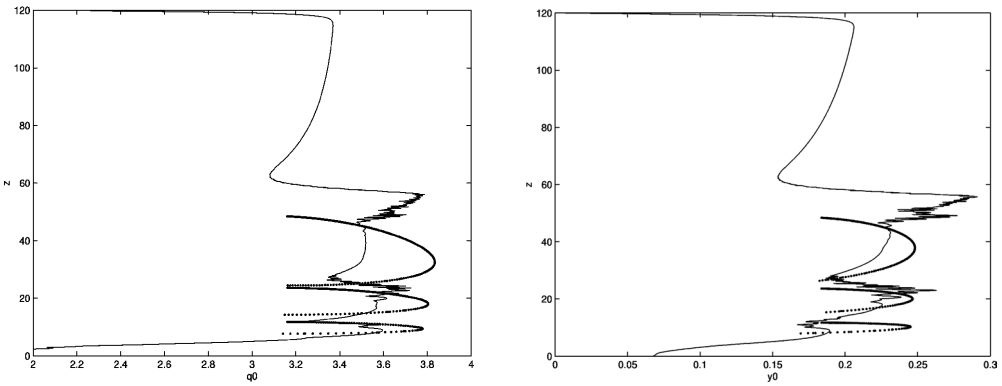

(a) (b)

Fig. 16. Oscillation amplitude distribution. Numerical simulation (thin line) and 1*st* order theoretical prediction (thick line). (a) Wake; (b) structure.

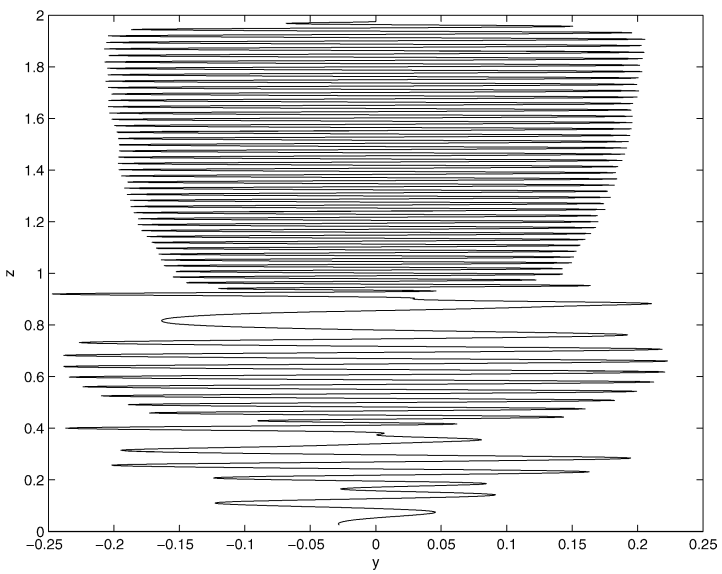

Fig. 17. Structure displacement snapshot.

6. Conclusions

A detailed investigation of elementary configurations of shear flow on a slender structure was carried-out. In the presence of wake diffusion, the dislocation cells were seen to enlarge the size of the lock-in region by merging onto its two ends. The extent of the lock-in region was also shown to be strongly related to the structure amplitude via the $U_r - y_0$ relationship plotted in Fig. 4. To a given structure amplitude corresponds a range of reduced velocity within which a local lock-in occurs.

In the most general case, a tensioned cable was studied and its response under incident shear flow was found to exhibit wave-packets distributed along its span. Those wave-packets were shown to result from a local lock-in. A local lock-in criterion, identical to that used in [19] for coupled oscillators, was shown to give a good prediction of the wake and structure amplitude along the cable. The role of the fluid damping term was demonstrated to essentially affect the envelop amplitude of the structure and wake motion without changing the global behavior of the system. In a more realistic case with a spatially-varying incident flow velocity, similar wave-packets patterns occurred and could also be interpreted using the same local lock-in approach.

References

[1] C.H.K. Williamson, R. Govardhan, Vortex-induced vibrations, Ann. Rev. Fluid Mech. 36 (2004) 413–455.
[2] R. Blevins, Flow-Induced Vibrations, van Nostrand Reinhold, 1990.
[3] J. Vandiver, Dimensionless parameters important to the prediction of vortex-induced vibration of long, flexible cylinders in ocean currents, J. Fluids Struct. 7 (1993) 423–455.
[4] J. Vandiver, D. Allen, L. Li, The occurrence of lock-in under highly sheared conditions, J. Fluids Struct. 10 (1996) 555–561.
[5] S. Balasubramanian, R.A. Skop, F. Haan, A. Szewczyk, Vortex-excited vibrations of uniform pivoted cylinders in uniform and shear flow, J. Fluids Struct. 14 (2000) 65–85.
[6] J. Morison, M. O'Brien, J. Johnson, S. Schaaf, The force exerted by surface waves on piles, Petroleum Transactions – AIME 189 (1950) 149–154.
[7] M.S. Triantafyllou, M.A. Grosenbaugh, Prediction of vortex-induced vibrations in sheared flows, in: Flow-Induced Vibration (Bearman), Balkema, 1995, pp. 73–82.
[8] C. Evangelinos, G.E. Karniadakis, Dynamics and flow structures in the turbulent wake of rigid and flexible cylinders subject to vortex-induced vibrations, J. Fluid Mech. 400 (1999) 91–124.
[9] C. Evangelinos, D. Lucor, G.E. Karniadakis, DNS-derived force distribution on flexible cylinders subject to vortex-induced vibrations, J. Fluids Struct. 14 (3–4) (2000) 429–440.
[10] D. Lucor, L. Iimas, G.E. Karniadakis, Vortex dislocations and force distribution of long flexible cylinders subjected to sheared flows, J. Fluids Struct. 15 (2001) 641–650.
[11] R. Willden, J. Graham, Numerical prediction of VIV on long flexible circular cylinders, J. Fluids Struct. 15 (2001) 659–669.
[12] C. Le Cunff, F. Biolley, E. Fontaine, S. Etienne, M.L. Facchinetti, Vortex-induced vibrations of risers: theoretical, numerical and experimental investigation, Oil & Gas Science and Technology 57 (2002) 59–69.
[13] G. Birkoff, E. Zarantanello, Jets, Wakes and Cavities, Academic Press, New York, 1957.
[14] R. Hartlen, I. Currie, Lift-oscillator model of vortex-induced vibration, J. Engrg. Mech. Div. 96 (EM5) (1970) 577–591.
[15] R. Skop, O. Griffin, On a theory for the vortex-excited oscillations of flexible cylindrical structures, J. Sound Vib. 41 (3) (1975) 263–274.
[16] P. Albarède, M. Provansal, L. Boyer, Modélisation par l'équation de Ginzburg–Landau du sillage tridimensionnel d'un obstacle allongé, C. R. Acad. Sci. Paris 310 (1990) 459–464.
[17] P. Monkewitz, Modeling of self-excited wake oscillations by amplitude equations, Exp. Therm. Fluid Sci. 11 (1996) 175–183.
[18] S. Balasubramanian, R.A. Skop, A nonlinear oscillator model for vortex shedding from cylinders and cones in uniform and shear flows, J. Fluids Struct. 11 (1997) 395–412.
[19] M.L. Facchinetti, E. De Langre, F. Biolley, Coupling of structure and wake oscillators in vortex-induced vibrations, J. Fluids Struct. 19 (3) (2004) 123–140.
[20] M.L. Facchinetti, E. De Langre, F. Biolley, Vortex-induced travelling waves along a cable, Eur. J. Mech. B Fluids 23 (2004) 199–208.
[21] M.L. Facchinetti, E. De Langre, F. Biolley, Vortex shedding modeling using diffusive van der Pol oscillators, C. R. Acad. Sci. Paris Ser. IIb 330 (2002) 1–6.
[22] S. Krenk, S.R.K. Nielsen, Energy balanced double oscillator model for vortex-induced vibrations, J. Engrg. Mech. 125 (3) (1999) 263–271.
[23] L. Mathelin, E. De Langre, F. Biolley, Vortex-induced vibrations and waves in shear flow, in: 8th Int. Conf. on Fluid-Induced Vibrations, École Polytechnique, Paris, France, July 6–9, 2004.